PAPER

Check for updates

Sustainable high-voltage source based on triboelectric nanogenerator with a charge accumulation strategy†

Rui Lei,[abc] Yuxiang Shi,[ab] Yafei Ding,[ab] Jinhui Nie,[ab] Shuyao Li, [ID][ab] Fan Wang,[ab] Hua Zhai,[c] Xiangyu Chen [ID] *[ab] and Zhong Lin Wang [ID] *[abd]

The application of TENGs as a controllable high-voltage power source is one of the four major research directions of TENGs. However, there are still many high-voltage applications beyond the driving capability of TENGs mainly due to the insufficient sustainability of tribo-induced charges. Here, we have proposed a triboelectric nanogenerator (TENG) with a charge accumulation strategy to provide a sustainable ultrahigh output voltage, which is enough to drive almost all the possible high-voltage applications of TENGs. More than 8000 LEDs can be continuously illuminated using this TENG device and the calculated output voltage from this device can reach over 20 kV, updating a new record for the TENG devices. The ultrahigh voltage from this TENG can trigger continuous electrophoresis (EP) and dielectrophoresis (DEP) effects in oil, achieving a self-powered oil purification system. The suspended impurities, including both conductive and dielectric particles, in 50 ml oil can be removed by this system within 100 seconds. This work offers a different purification system for the current oil recycling industry with a simple design and zero power consumption. Meanwhile, two kinds of typical high-voltage devices, a dielectric elastomer actuator (DEA) and electrospinning system, can be directly driven by this SH-TENG with a rather low rotation speed, while no power source or amplifying circuit is needed. All of these demonstrations verify that this new type of TENG can provide some practical applications in many fields such as electrostatic manipulation and air pollution treatment.

Broader context

Triboelectric nanogenerators (TENGs) are a leading candidate among various harvesting techniques and the application of TENGs as controllable high-voltage power sources is one of the four major research directions. However, the maximum transferred charge from TENGs is a limited value, which means the high output voltage from TENGs is usually a pulse signal with insufficient sustainability. If we can provide a sustainable output voltage larger than 20 kV, we can support almost all kinds of high-voltage applications using TENGs. In this work, a different type of TENG using a charge accumulation strategy to boost the output voltage was developed, and it can provide a sustainable output voltage over 20 kV, indicating an unprecedented output capability. For demonstration, two kinds of typical high-voltage devices, namely, the dielectric elastomer robotics and electro-spinning system, can be easily driven by this TENG with good performance. Moreover, for the first time, the TENG device is able to drive the purification system for industrial oil purification, which can satisfy the global needs of energy conservation and environmental protection. The proposed TENG as a stable ultrahigh-voltage source can strongly promote the practical application of TENGs.

[a] CAS Center for Excellence in Nanoscience, Beijing Key Laboratory of Micro-nano Energy and Sensor, Beijing Institute of Nanoenergy and Nanosystems, Chinese Academy of Sciences, Beijing 100083, P. R. China. E-mail: chenxiangyu@binn.cas.cn

[b] School of Nanoscience and Technology, University of Chinese Academy of Sciences, Beijing 100049, P. R. China

[c] Anhui Province Key Lab of Aerospace Structural Parts Forming Technology and Equipment Institute of Industry & Equipment Technology, HFUT, Hefei 230009, P. R. China

[d] School of Material Science and Engineering Georgia Institute of Technology, Atlanta, GA 30332-0245, USA. E-mail: zhong.wang@mse.gatech.edu

† Electronic supplementary information (ESI) available. See DOI: 10.1039/d0ee01236j

Introduction

As a leading candidate among various harvesting technologies, triboelectric nanogenerators (TENGs) have been demonstrated to have tremendous application prospects in many fields such as energy harvesters,[1–5] active sensors,[6–9] human–machine interfaces,[10–12] and portable power sources.[13–17] TENGs can instantly convert mechanical energy to electricity with very high energy conversion efficiency, while the material selection and the structure design of TENGs can be very flexible, indicating

the unprecedented advantages of lightweight, low cost and universal applicability.[18–23] Relying on the electrostatic induction effect,[24–27] TENGs can generate an extremely high electrostatic field and their open-circuit voltage (V_{OC}) can easily reach few thousand volts.[28–32] However, the maximum transferred charge of TENGs is a limited value, which means that the high-output voltage from TENGs decays quickly. Usually, a single-electrode TENG with a good insulating material can achieve an instant output voltage larger than 2 kV, while a free-standing type TENG with a large tribo-surface can generate an instant voltage of 15 kV.[33] However, these voltage values can only be maintained for 1–2 seconds due to the relaxation of electrostatic charges.[34] Charge accumulation is an effective way of enhancing the performance of the TENG device.[35,36] By introducing a charge supplement channel to a multilayer TENG,[37] a stabilized output voltage of 7 kV can be produced, which is so far the highest value for the device at this size. Meanwhile, the further increase in the voltage value is also limited by this multilayer structure. However, the voltage multiplier rectifying circuit[38,39] is also a possible strategy for amplifying the output voltage from a rotating-type TENG.[40] Nevertheless, the charging process of the capacitors in the multiplier circuit by using TENGs is not sufficient and thus, the highest output voltage from this kind of multiplier rectifying circuit is usually a limited value.[38,39] The application of TENGs as a controllable high-voltage power source is one of the four major research directions of TENGs.[41] Several kilovolt output voltage can be directly provided by using TENGs, which is enough to drive many electrically responsive devices, including dielectric/piezoelectric actuators,[42,43] ferroelectric memorizers,[44] electrostatic manipulators,[28] electrostatic air cleaners,[45] and field emitters.[46] With the help of multiplier circuits, the TENG devices can even drive electrospray[47] and electrospinning devices.[38] However, there are still many high-voltage devices and applications beyond the driving capability of the current TENG system. For example, oil purification technique based on electrophoresis (EP)[48,49] and dielectrophoresis (DEP)[50–52] effects is very useful for releasing the growing problem of water and environmental pollutions. A high-voltage source is necessary for triggering the EP or DEP process, and TENGs can be the preliminary candidate to replace the voltage source for the oil purification system, which may simplify the complexity of the system and further reduce the cost for the operation. Unfortunately, the driving voltage of DEP (or EP) for oil purification is usually larger than 10 kV, which is higher than the previous record of sustainable voltage output from TENGs. Hence, it is still necessary to further elevate the sustainable voltage output of TENGs, in order to satisfy the demands of various ultra-high-voltage applications.

Herein, a unique type of TENG using a charge accumulation strategy to boost the output voltage is developed, which can provide a sustainable output voltage over 20 kV. Two charge accumulators with very small inherent capacitance are designed to build up a very high electrostatic field. Meanwhile, the continuous motion of transporting-electrodes on a rotating disk can transfer charges to accumulators, which helps to replenish the charge leakage from accumulators. Accordingly, more than

8000 light-emitting diodes (LEDs) are continuously lighted up using this sustainable high-voltage TENG (SH-TENG), indicating an unprecedented output capability. More importantly, this SH-TENG realizes a self-powered oil purification system based on the coupling effects of DEP and EP, which can remove the suspended impurities in 50 ml oil within 100 seconds. The combination of self-powered TENG technique and the DEP (or EP) system can simplify the complexity of the system and further reduce the cost for the operation, which may offer a new approach for the current oil recycling industry. Moreover, two kinds of typical high-voltage devices, the dielectric elastomer actuator (DEA) and electrospinning system, can be directly driven by this SH-TENG at a rather low rotation speed, which shows promising applications of this TENG in the field of high-voltage manufacturing equipment and artificial muscle.

Results and discussion

Structure design and working mechanism of SH-TENG

The simplified 3D structural scheme of the SH-TENG is illustrated in Fig. 1a and b. The polarizer, disk, transmission bridge and a pair of accumulators are designed to establish the main part of the SH-TENG, while the continuous output is generated by the rotation of disk. The polarizer consists of two fan-shaped triboelectric films with opposite electrification polarity (Kapton and Nylon),[53] which can generate a strong electrostatic field to support the induction process. Theoretically, the triboelectric materials with opposite electrification polarity can be selected for the device and we list the possible choices as in Table S1 (ESI†). Combining with the supporting plastic, the foam is adhered to the back side of the dielectric
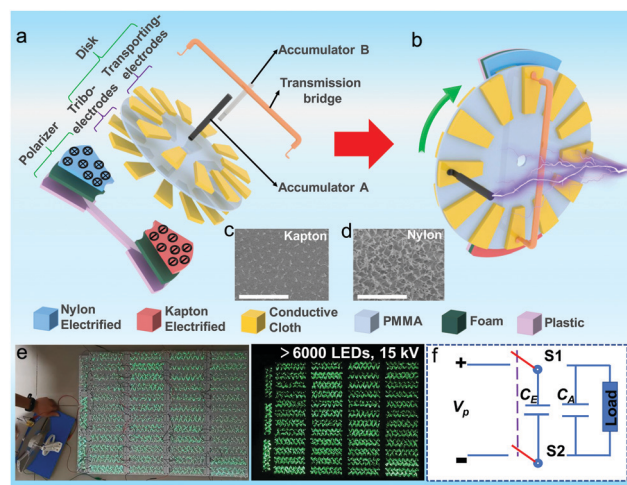

Fig. 1 Structural design and demonstrations of the SH-TENG as a practical power source. (a) Exploded schematic of the SH-TENG, and the diameter of the disk is 230 mm. (b) Assembly structural illustrations of the SH-TENG. (c) SEM image of the etched nanostructures on the Kapton surface, and the scale bar is 10 μm. (d) SEM image of the etched nanostructures on the nylon surface. (e) More than 6000 LEDs are lighted up by the SH-TENG with hand-power. (f) Equivalent circuit model of the SH-TENG.

layers, ensuring effective contact between the polarizer and the disk.

Meanwhile, the surface of Kapton and nylon is etched with nanostructures by inductively coupled plasma (ICP) emission spectroscopy, to maintain a larger effective surface area and a higher triboelectric charge density. The scanning electron microscopic (SEM) image is shown in Fig. 1c and d. Each electrode array is composed of 12 sectors with a central angle of 15°, which are radially arrayed in a circular form with equal degrees and are fully imbedded on the PMMA surface. It is important to note that the two electrode arrays have different functions. The tribo-electrodes array on the backside of the disk (rubbing with polarizer) can confirm that the surface charge density on the dielectric layer is always a saturated value, while the other electrode array on the top of disk (transporting-electrodes) is able to transfer the charges (induced by polarizers) to the accumulators. The transmission bridge is fixed above the polarizer, and the pair of accumulators is fixed vertically to the transmission bridge. Each end of the transmission bridge and the accumulators are periodically contacted with transporting-electrodes when the disk is rotating. The transmission bridge and the pair of accumulators have flexible wires at the end, which can ensure the good contact with the transporting-electrodes. It is noteworthy that the contact area between the transmission bridge and the rotating disk is very small. Even though the sliding motion on transmission bridges on the surface of the disk may cause some electrification effects, it is still negligible in comparison with the output signal. The fabrication process is discussed in detail in the Methods section, and the complete assembly of equal scale model for SH-TENG is shown in Fig. S1 (ESI†). To facilitate the manual operation of SH-TENG, a belt transmission mechanism with a handle is used to increase the rotation speed of the disk (the speed increase rate is 4:1), as shown in Fig. S1d (ESI†). As can be seen in Fig. 1e and Video S1 (ESI†), more than 6000 LEDs connected in a series are illuminated by this SH-TENG. The sustainable output voltage of this SH-TENG is at least more than 15 kV. (Another demonstration with 8000 LEDs is shown in the later part.) An equivalent circuit of SH-TENGs based on charging and discharging capacitors is also proposed in Fig. 1f, where the electrified polarizer can be simplified as the power source V_P. The pair of electrified trans-porting electrodes (electrode A and electrode B, as shown in Fig. 2) can be considered as the two plates of the capacitor C_E with low capacitance (due to the parallel position of the two plates in one panel), while the inherent capacitor of the accumulators as well as the capacitor of external loads can be regarded as C_A. The opening and closing of switches S1 and S2 represent the moving of transporting-electrodes from the transmission bridge to accumulators during the rotation of the disk.

The working mechanism of this SH-TENG (see Fig. 2) is little bit different from the conventional TENG configuration. The relative rotation between the disk and the polarizer can help to maintain the saturated surface charge density on the Nylon and Kapton surface, while the detailed triboelectrification process between tribo-electrodes and dielectric layers is shown in Fig. S2–S4 (ESI†) and the discussion in Note S1 (ESI†).
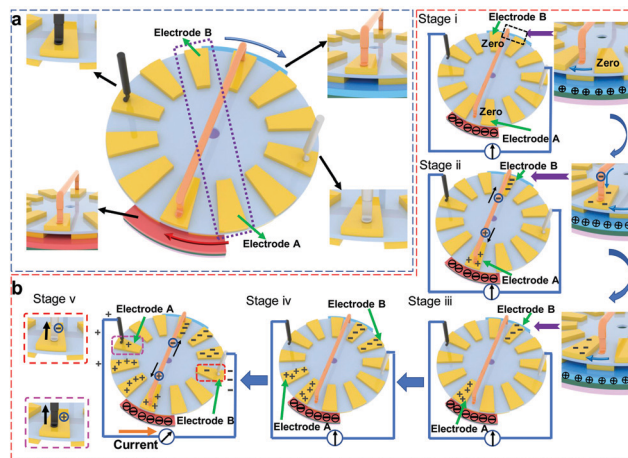

Fig. 2 Schematics of operating principle of the SH-TENG. (a) Initial state in which electrodes A and B are not in the dielectric layer coverage area. (b) Schematic showing the proposed working principle of the SH-TENG with the electron flow diagram in five consecutive stages within a full cycle of current output.

The projection of two-electrode arrays (tribo-electrodes and transporting-electrodes) in the axial design is completely complementary without overlapping. Therefore, the charges on the tribo-electrode do not affect the charges on the transporting-electrode (they are perfectly dislocated). The energy generation process of this SH-TENG (see Fig. 2b) can be divided into five stages as the disk rotates in the clockwise direction. To simplify the discussion, we pick a pair of axisymmetric transporting-electrodes (named electrode A and electrode B) for demonstration, as shown in Fig. 2a. In stage i, the transporting-electrodes are moving towards the transmission bridge. The transporting-electrodes are isolated before they establish contact with the transmission bridge and the total charge on them should be close to zero. In stage ii, the transporting-electrodes are connected with the transmission bridge and the charges with different polarities move across the bridge to accumulate on the transporting-electrodes. The positive (negative) charges are induced on the electrode above the Kapton (Nylon) film. Owing to the high electrostatic field generated by a polarizer, positive charges are accumulated on electrode A and negative charges are transferred to electrode B. In stage iii and iv, the induced charges are carried by transporting-electrodes towards the accumulators during the rotation of the disk and new charges are continuously induced on the successive electrodes. Finally, when electrode A (B) is fully in contact with accumulator A (B) in stage V, the electrostatic charges are stored on the accumulators, establishing a high output voltage. The continuous rotation of the disk helps to compensate the charge leakage on the accumulators, and the high output voltage from this SH-TENG can be maintained. Thus, the entire process can result in a unidirectional output with the rotation of the disk. The equivalent circuit of the whole system also has two procedures: the charging and the discharging (Fig. S5, ESI†). In the charging procedure (Fig. S5a, ESI†), when the pair of transporting-electrodes get in touch with the transmission bridge, the induced

charges on electrode A and electrode B are q and $-q$ without considering the edge effects. The discharging procedure (Fig. S5b, ESI†) can be simplified under the open-circuit condition, where the two transporting-electrodes act as capacitors to charge the capacitor related to the two accumulators. In real experiments, external loads are connected to accumulators and C_E would be much smaller than C_A (the series connection of the inherent capacitor between accumulators A and B and the capacitor of external loads). Hence, almost all the charges on transporting-electrodes are transferred to the accumulators during the contact, and the amount of charges on accumulators (Q_A) can be presented by the following integer-valued function:

$$Q_A = \left[\frac{Nnt}{60}\right] \cdot q \tag{1}$$

where N is the total number of transporting-electrodes, q a fixed value related to the charges on each transporting-electrode and n (rpm) the rotation speed of disk (see Note S2, ESI†). Theoretically, the increase in Q_A is limited by the charge leakage effect. The charge leakage on the accumulators becomes faster with the increase in the accumulated charge amount, while this leakage phenomenon can be approximately modelled based on some empirical equations.[54] In this case, the leakage charge can be estimated using the following equation:

$$Q_{leakage} = \int_0^t \left[\frac{Nnt}{60}\right] \cdot q \cdot A e^{\left(\left[\frac{Nnt}{6}\right] \cdot \frac{q}{Q_B}\right)} dt \tag{2}$$

where Q_B is an empirical constant and A the leakage coefficient related to the conductivity of the leakage path. The charge leakage increases slowly with a small amount of Q_A, while the charge leakage increases exponentially with a larger Q_A. The remaining charges on accumulators are the difference between Q_A and $Q_{leakage}$, and the V_{OC} can be briefly obtained using the following equation:

$$V_{OC} = \left\{ \left[\frac{Nnt}{60}\right] \cdot q - \int_0^t \left[\frac{Nnt}{60}\right] \cdot q \cdot A e^{\left(\left[\frac{Nnt}{6}\right] \cdot \frac{q}{Q_B}\right)} dt \right\} \cdot \frac{1}{C_A} \tag{3}$$

It is important to note that the charge leakage rate is in proportion to the amount of accumulated charges. Hence, with the increase in accumulated charges, the charge amount on accumulators can reach a maximum value (maximum V_{OC}), when the charge compensation is just balanced with the charge leakage. The detailed deduction process of the above equation is displayed in Note S2 (ESI†).

Output performance of SH-TENG

To measure the electrical performance of SH-TENGs, a stepper motor is employed to ensure the stable and continuous rotation of the disk. We set the rotation speed of the motor at 50 rpm and measure basic output of SH-TENG. To further ensure the mechanical stability of SH-TENG, the thickness of the disk is fixed at 3 mm. Although the disk keeps rotating, the transporting-electrode array and accumulators always contact first and then separate, as shown in Fig. 3a, resulting in the stepwise increase in charges on the accumulators (see Fig. 3b). Each transporting-electrode can provide a charge amount of 19.7 nC.

Similarly, with the disk moving 1 step, the V_{OC} increases by 70 V (Fig. 3c), and as the disk rotates, the V_{OC} continues to rise. To theoretically predict the distribution of the electrical potential between the transporting-electrodes, COMSOL simulation that employs the finite element method (FEM) is implemented. As shown in Fig. S6 (ESI†), the calculated electrical potential difference between the two transporting-electrodes at the location of accumulators is about 25 kV. The peak value of the short-circuit current (I_{SC}) of SH-TENGs is about 10.1 μA,
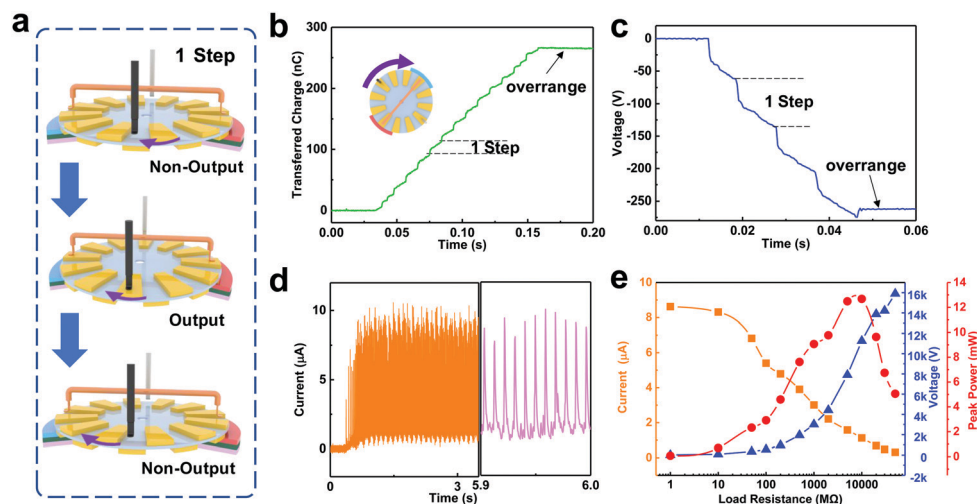

Fig. 3 Output performance of the SH-TENG at 50 rpm. (a) Schematic of the disk moving 1 step. (b–d) Transferred charge, V_{OC} and I_{SC} of the SH-TENG when the device continuously rotates. (e) Dependence of the output current, voltage and peak power on different resistive loads.

as illustrated in Fig. 3d. The dependence of the V_{OC}, I_{SC} and peak power on external resistance is given in Fig. 3e. Since the internal resistance of the SH-TENG is large, a maximum peak power of 12.68 mW can be obtained under an external resistance of 10 GΩ and this matching resistance is much larger than other common TENG devices (usually the corresponding external resistance is from 0.5 MΩ to 300 MΩ). Meanwhile, as can be seen in Fig. 3c, the V_{OC} is beyond the detection range of the voltage meter (Keithley 6514) after the disk only moves 4 steps. Therefore, we have to use another method to estimate the value of V_{OC}. When the SH-TENG is connected to a large external resistance (50 GΩ), it can be regarded as an open-circuit state, and the voltage measured in this state can be used as V_{load}, and it is calculated by the equation $V_{load} = IR$, where I is the short circuit current through the external resistance (R) of 50 GΩ. The measured voltage is 15.9 kV, which is close to the estimated voltage from lighting 6000 LEDs.

The rotation speed of the disk is a main factor that influences the electrical outputs of SH-TENG, and the maximum rotation speed for the stable operation of SH-TENG is around 90 rpm. It should be noted that the amount of charge carried by each transporting-electrode is fixed (Fig. S7, ESI†), so the

increase in rotation speed only accelerates the rate of charge replenishment to the accumulators. When the speed of the stepper motor increases from 10 rpm to 90 rpm, the peak value of I_{SC} increases slowly from 6.64 μA to 11.67 μA, as can be seen in Fig. 4a. Here, two parameters are considered to study the performance I_{SC}: the peak value and the valley value of current (see Fig. 4a). The inset in Fig. 4a gives a sample of I_{SC} of SH-TENGs, when the rotation speed is 90 rpm. With the increase in rotation speed, the valley value of current increases from 0 μA to 1.26 μA, indicating the enhanced charge replenishment from transporting-electrodes to accumulators. To better explain the relationship between the valley value and the rotation speed, we proposed an illustration, as shown in Fig. S8 (ESI†). High rotation speed means higher frequency of the current signal. The schematic of each signal with low frequency to generate a low valley value is shown in Fig. S8a (ESI†). No overlapping between different signals under low frequency and the valley value is close to zero. With the increase of frequency, signals can overlap with each other which lifts the valley value, generating a continuous signal, as shown in Fig. S8b (ESI†). The increase in valley current confirms that the charge is constantly transferred to accumulators without interruption. Hence, we can consider the device as a
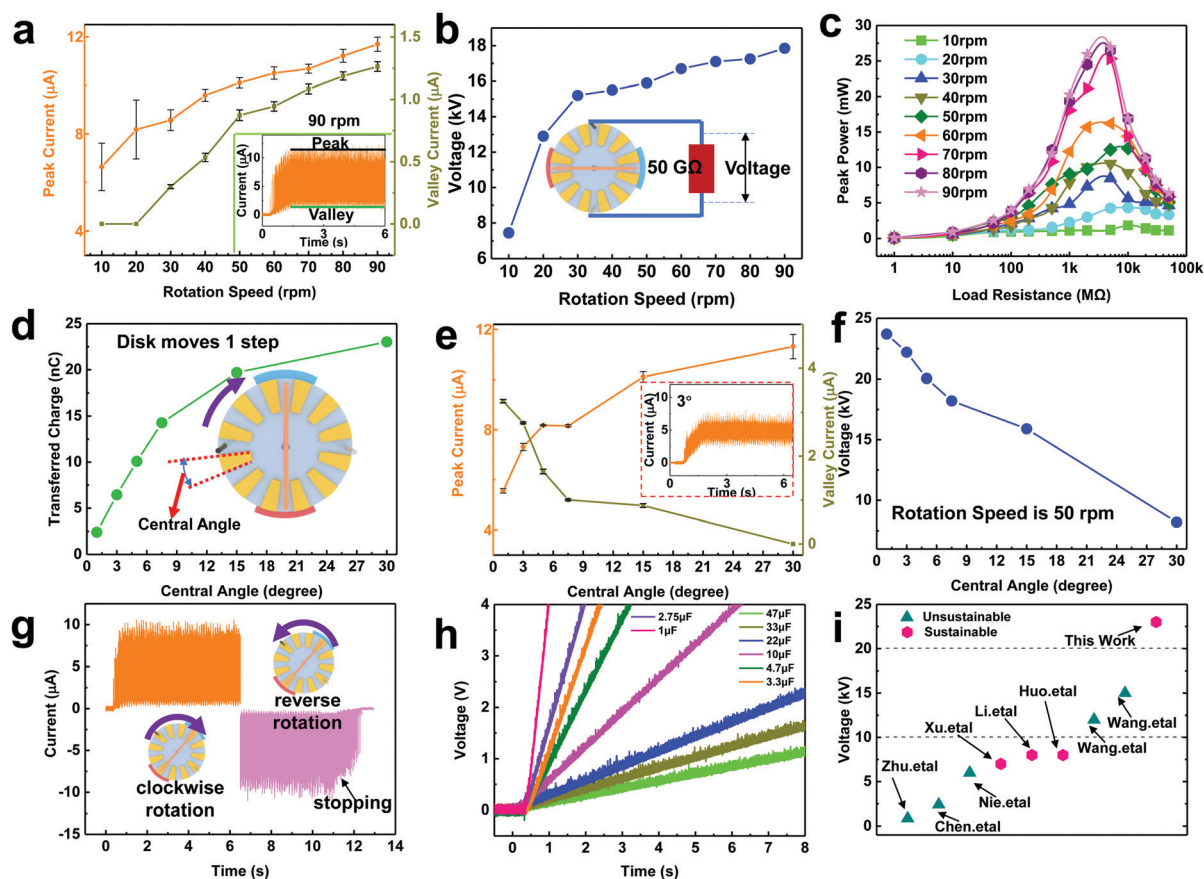

Fig. 4 SH-TENG performances with different parameters and stimuli. (a–c) Dependence of I_{SC}, measured output-voltage, peak power at different rotation speeds (the central angle is 15°), respectively; error bars represent the standard deviation based on eight replicate data. (d–f) Dependence of the transferred charge, I_{SC}, measured output-voltage on different central angles (the rotation speed is 50 rpm), respectively. (g) Dependence of I_{SC} when the disk rotates clockwise or anti-clockwise at 50 rpm. (h) Charging voltage curves for different capacitors with the SH-TENG direct connect with the capacitor. (i) Comparison with other high-voltage TENGs.

sustainable source. With the increase in rotation speed, the valley value of current is increased, and this value may also be decided by the sampling frequency of a Keithley 6514 System Electrometer.

At the same time, by increasing the rotation speed, the measured voltage across 50 GΩ gradually increases and a maximum voltage of 17.85 kV is obtained at 90 rpm (see Fig. 4b). Accordingly, the maximum peak power of 26.9 mW is captured at 5 GΩ when the rotation speed is 90 rpm, and the energy density of these triboelectric films is correspondingly calculated to be 4.28 mW m^{-2} (surface density) and 85.4 kW m^{-3} (volume density). The power density is higher than the energy density of the piezoelectric generator (9 kW m^{-3}).[55] Moreover, the power-weight ratio whole device, including the disk and the accumulator (about 148 g), is 181.7 mW kg^{-1}, which is also larger than the common electromagnetic generator (0.25 mW kg^{-1}).[56] The efficiency of the SH-TENG is calculated to be 17.3%, as explained in Note S3 (ESI†). It is important to note that the duration of this SH-TENG is not strongly influenced by the lifetime of nano/micro structures on the surface. After 10 thousand motion cycles, the micro/nano structures on the film are totally destroyed. However, the Kapton and nylon are still durable without tearing or other damages (the rotation rate of the motor is 50 rpm), as shown in Fig. S9 (ESI†) by SEM observation. Meanwhile, the peak value of short-circuit current (I_{SC}) of the SH-TENG is about 8.5 μA, as illustrated in Fig. S10 (ESI†), and the transferred charge of one motion step is decreased to 17 nC (Fig. S11, ESI†), which means at least 80% of the output performance can be still maintained.

The dependence of the V_{OC}, I_{SC} and peak power on external resistance is shown in Fig. S12 (ESI†), where the output power is decreased around 30%. Usually the nanostructures on the surface can significantly enhance the performance of TENGs in a contact separation mode. In our case, the electrification part is in a sliding mode with multiple electrodes. Hence, the contribution of the nanostructures on the surface is not so significant.

However, the central angle of transporting-electrodes is the most important structural parameter to decide the output performance of the device. In order to obtain more accurate measurement data, we employed the printed circuit board (PCB) technology to fabricate thinner electrodes. To clarify the influence of different central angles on the output performance, the rotation speed is fixed to be 50 rpm, and the output characteristics of the SH-TENG devices with central angles of 1°, 3°, 5°, 7.5°, 15° and 30° are illustrated respectively in Fig. 4d–f. The transferred charges with 1 motion step of the disk gradually increase with the increase in central angle (see Fig. 4d), suggesting that the transferred charges from one electrode are in proportion with the overlapping area of the electrode. However, due to the edge effort, the charge density gradually decrease with the increase in central angle (larger overlapping area). The peak value of I_{SC} gradually increases from 5.56 μA to 11.31 μA with the increase in central angle (from 1° to 30°), as illustrated in Fig. 4e and Fig. S13 (ESI†). The increasing amount of the charges on single electrodes can generate an instant current ($I_{SC} = \mathrm{d}Q/\mathrm{d}t$), when the accumulator

is contacted with transporting-electrodes. With the decrease in central angle, the contact frequency between transporting-electrodes array and accumulators is increased, which accelerates the charge transfer rate and leads to an increase in the valley value of I_{SC}. As can be seen in Fig. 4e, the valley value of I_{SC} gradually increases from 0 μA to 3.25 μA with the decrease in central angle (from 30° to 1°). Hence, as the central angle decreases, the charge replenishment is more sustainable. The measured voltage across 50 GΩ increases gradually with the decrease in central angle and the voltage reaches the maximum value of 23.7 kV, when the central angle is 1° (Fig. 4f). To further verify this calculated voltage, 8000 LEDs are lighted up continuously, as demonstrated in Fig. S14 (ESI†).

The size of the polarizer is another structural parameter to decide the output performance of the device. The original size of the polarizer in the manuscript is fixed with a central angle of 46°. To further study the effect of the size of the polarizer, the output performance of the SH-TENG is tested with a central angle of polarizer at 31° and 16° (the central angle of the electrode is 15° and the rotation speed is 50 rpm). The output performance of the SH-TENG with different central angles of the polarizer is shown in Fig. S15 (ESI†). The output performance is not affected so much with the central angle of the polarizer at 31°. However, when the central angle of the polarizer is decreased to be 16°, the output performance of the SH-TENG is decreased slightly. The peak value of short-circuit current (I_{SC}) of the SH-TENG is about 8.35 μA, the transferred charge of one motion step is decreased to 16.7 nC, and the measured output-voltage is reduced to 12.35 kV, which means about 80% of the output performance is maintained. This result indicates the edge effect on the output performance of the SH-TENG when the size of the electrode is close to the size of the polarizer.

It is worth noting that, if one of the triboelectric materials is removed, the SH-TENG can still work, but the output performance is suppressed accordingly. The high electrostatic field can still be generated by the polarizer with a single triboelectric material when the disk rotates. The corresponding experiments on the output performance of the SH-TENG with one triboelectric material were conducted (the central angle of the electrode is 15° and the rotation speed is 50 rpm), and the corresponding output performance of the SH-TENG is shown in Fig. S16 (ESI†). When the Kapton (Nylon) is remained (removed), the peak value of short-circuit current (I_{SC}) of SH-TENG is about 7.1 μA, the transferred charge of one motion step is about 12.8 nC, and the measured output-voltage is about 11.2 kV. This means only about 70% of the output performance can be maintained if Nylon is removed. While Nylon (Kapton) is remained (removed), only about 40% of the output performance of the SH-TENG can be maintained.

Furthermore, when the disk rotates in the anticlockwise direction, the polarity of the output voltage from the SH-TENG is reversed, as shown in Fig. 4g. To further demonstrate the ability of the SH-TENG as a unidirectional power source, a total of 240 LEDs were used as the external load. All the LEDs were divided into two groups on two breadboards respectively

(see Fig. S17, ESI†): 120 LEDs in group 1 (left side) were lighted up by the TENG in clockwise direction, while no light emission can be observed from the other group (right side). Moreover, when the rotation direction of the SH-TENG is reversed, only the LEDs of group 2 can be lighted up. The SH-TENG can be used as a power source to directly charge the capacitors without a rectifier bridge, as can be seen in Fig. S18a (ESI†). Fig. 4h shows the voltage signal of different capacitors charged by this SH-TENG, that is, a capacitor of 22 μF can be charged to 2 V within 8 s, which is comparable to the charging efficiency of the reported TENG device with a charge accumulation strategy.[35] The charging efficiency of this system can be further improved by increasing the rotation speed and using a smaller capacitor (see Fig. S18b, ESI†). The results indicate that the SH-TENG can be directly used as an efficient power source. In the past, there were a series of studies focusing on boosting the stable output voltage from the TENG,[30,33,34,37–40,57] as summarized in Fig. 4i. Before our study, the highest sustainable output voltage based on the TENG device was around 8 kV, which was achieved by integrating a voltage multiplier rectifying circuit and a freestanding-rotating TENG.[38,39] Nevertheless, the highest output voltage from this kind of multiplier rectifying circuit is

a limited value (usually around 8 kV), which is due to the insufficient charging process of the capacitors using the TENG. Moreover, the multiplier circuit itself consumes a certain amount of energy, which can be a burden for the TENG. However, some studies have also reported an output voltage larger than 15 kV,[57] while it is just a pulse signal but not a sustainable output. In comparison with the previously reported works (see Fig. 4i and Table S2, ESI†), this SH-TENG can provide the highest sustainable output voltage, which is enough for supporting almost all kinds of high-voltage applications.

Application of SH-TENG for oil purification

Based on its sustainable high voltage, the application of this SH-TENG can be extended to a new field of oil purification, which relies on the combined effects of EP and DEP. The EP enables the separation of a variety of biological and chemical substances with electrostatic charges.[48,49] Meanwhile, the DEP can collect tiny particles by utilizing the force exerted by a nonuniform electric field on a polarizable particle, while it is irrelevant with the charges on particles.[50,58,59] The system relying on the EP and DEP effect can effectively remove the impurities from the oil, which is time efficient and cheaper
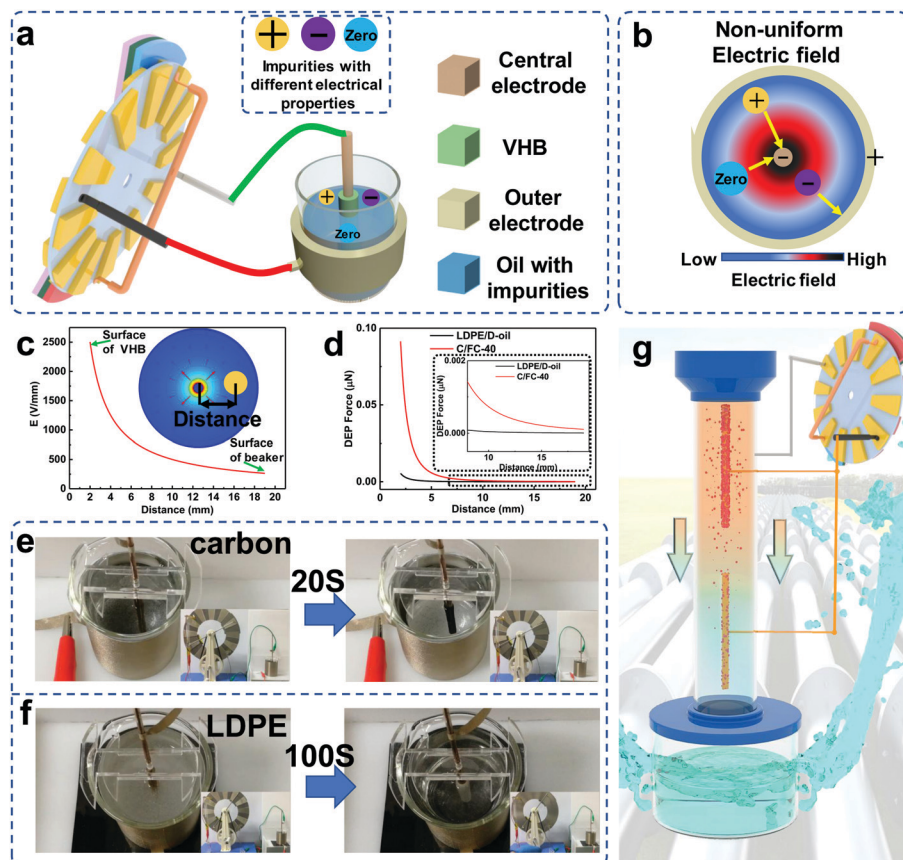

Fig. 5 Oil purification system and its practical effect demonstration. (a) Schematic of oil purification system. (b) Electric field distribution profile inside the cell. (c) Non-uniform field strength from the central electrode to the outer wall. (d) In the non-uniform electric field, the calculation results of dielectrophoretic force with a single impurity at different distances from the central electrode. (e) Photograph of the SH-TENG to purify the dispersed carbon in the FC-40 oil within 20 s. (f) Photograph of the SH-TENG to purify the dispersed LDPE in dimethyl silicone oil within 100 s. (g) Prospect of the SH-TENG for industrial filtration applications.

than the method using a molecular sieve. The systematic concept of the oil purification system is described in Fig. 5a, where the system consists of two functional parts, including the SH-TENG as the power source and the separating part to adsorb the suspended impurities in the oil. The separating part consists of a Cu columnar electrode (diameter: 2 mm) covered with a VHB tape (thickness: 1 mm), a beaker (volume: 50 ml; diameter: 40 mm) containing oil, and a conductive cloth as the outer electrode adhered on the outer wall of the beaker. Accumulator A is connected to the outer electrode, while accumulator B is connected to the central electrode. Then 50 ml oil liquid mixed with different particles as impurities is taken in the beaker, while the rotation of the SH-TENG can generate a high-voltage output between two electrodes to purify all the impurities. Owing to the coaxial design of the electrodes, a divergent non-uniform electric field is generated, as shown in Fig. 5b, and the electric field strength E at a distance r from the central electrode can be calculated using eqn (4):

$$E = \frac{r^0 \cdot (V_{OC})}{\ln(r_1/r_2)} \cdot \left(\frac{1}{r}\right) \tag{4}$$

where r_1 is the radius of the central electrode, r_2 the radius of the outer electrode, and r^0 the unit radius vector. Furthermore, the electric field can be expressed by the following formula with the consideration of dynamic V_{OC}:

$$E = \frac{r^0}{\ln(r_1/r_2)} \cdot \left(\frac{1}{r}\right)$$
$$\times \left\{ \left[\frac{Nnt}{60}\right] \cdot q - \int_0^t \left[\frac{Nnt}{60}\right] \cdot q \cdot A\sigma_{air} e^{\left(\left[\frac{Nnt}{6}\right]\frac{q}{Q_B}\right)} dt \right\} \cdot \frac{1}{C_A} \tag{5}$$

The non-uniform field strength from the central electrode to the outer electrode was calculated, as shown in Fig. 5c. In the case of the manually rotating SH-TENG, the applied V_{OC} of the SH-TENG is considered to be about 15 kV. The rational designed non-uniform electric field enables an electric field strength of >2.5 kV mm^{-1} near the center electrode. The particle filtering process relies on the combined effects of EP and DEP.

The mixed particles may naturally carry some charges and these pre-charged particles are continuously subjected to electric field force F_e, which drives them to move towards either electrode in the system, as shown in Fig. 5b. This is related to the EP effect, and the related electric field force F_e acting on a single charged particle can be calculated based on the effective net charge q_1 of the particle as: $F_e = Eq_1$, and the electric field force F_e is calculated in Fig. S19a (ESI†), where the charge density of particles is 1 μC m^{-2} and the applied V_{OC} from the SH-TENG is 15 kV.

However, for most impurities in the oil, there is no charge on its surface and the DEP force F_d induced by non-uniform electric field can help to collect these particles, as described in Fig. S19b (ESI†). The translational force can cause motion of

neutral particles toward the concentrated local field strength, which is the central columnar electrode in our system, and the VHB tape covered on the central electrode can help to capture all the approaching particles. A mathematic method for calculating the DEP force has been proposed in a previous work.[50,58] DEP force F_d can be calculated by $F_d = \mu \cdot \nabla E$, where μ is the effective dipole moment of a spherical particle embedded in a dielectric medium. The effective dipole moment μ can be calculated using the following equation:

$$\mu = -4\pi a^3 \varepsilon_0 K_1 \cdot \frac{K_2 - K_1}{K_2 + 2K_1} \cdot E \tag{6}$$

The DEP force F_d affected on the single dielectric particle can be described in (7) as follows:

$$F_d = -4\pi a^3 \varepsilon_0 K_1 \cdot \frac{K_2 - K_1}{K_2 + 2K_1}$$
$$\cdot \frac{\left\{ \left[\frac{Nnt}{60}\right] \cdot q - \int_0^t \left[\frac{Nnt}{60}\right] \cdot q \cdot A\sigma_{air} e^{\left(\left[\frac{Nnt}{60}\right]\frac{q}{Q_B}\right)} dt \right\}^2}{r^3 \left(\ln \frac{r_1}{r_2}\right)^2 C_A^2} \cdot r^0 \tag{7}$$

where a is the radius of the single dielectric particle, ε_0 the vacuum permittivity, and K_1 and K_2 the relative permittivity of the oil medium and dielectric particles. Based on this theory, the DEP force of the carbon black filler (CBF) in Fluorinert FC-40 liquid (referred as FC-40) solution can be estimated, as shown in Fig. 5d. Meanwhile, the DEP force of low-density polyethylene (LDPE) in dimethyl silicone oil (D-oil) can also be obtained based on the similar calculation. As shown in Fig. 5d, the DEP force of CBF in FC-40 is much higher than that of LDPE in D-oil, which is attributed to the higher permittivity K_2 of CBF (conducting material). As can be seen in Fig. S19a (ESI†), the DEP force is much smaller than the EP force, but the DEP force is indispensable for the system, since this force can collect particles without surface charges. The motion of suspended particles in oil liquid is also subjected to the viscous drag force of F_v, which can be a negative effect for the purification system. The magnitude of the viscous drag F_v, according to the Stokes equation is

$$F_v = 6\pi\eta av \tag{8}$$

where η is the viscosity of the oil medium and v the velocity of the particle through the oil medium. The maximum velocity v_{max} of a single impurity at the distance r from the central electrode is achieved when translational force balances with viscous drag F_v. Combining eqn (7) and (8), the maximum velocity v_{max} of impurities driven by translational force F_d is obtained, as shown in Fig. S19c and d (ESI†). According to the calculated velocity, the moving speed of particles suspended in the oil increases exponentially near the central electrode.

It is quite difficult to separate the CBF from the oil liquid by a nonelectrical method such as filtration or centrifugation.[58] However, using EP and DEP technology, the separation of CBF from oil liquid becomes simple and effective. By stirring fifty milligrams of CBF into the transparent FC-40, the liquid

became a cloudy and homogeneous mixture and then poured into the beaker, as presented in Fig. 5e. The central electrode of the oil purification system is negatively charged, while the outer electrode is positively charged, due to the rotation of the SH-TENG. The dispersed CBF in the liquid quickly migrates towards the central electrode to form a coating. Meanwhile, the oil liquid becomes very clear within 20 seconds, as presented in Fig. 5d and Video S2 (ESI†). The particle velocity observed from Video S2 (ESI†) is in accordance with the estimation presented in Fig. S19c (ESI†) (the velocity increases from 1 mm s^{-1} to 25 mm s^{-1} in the direction towards the central electrode), suggesting that the DEP force dominates the collection of CBF particles. For the case of oil mixed with LDPE (100 mg), almost all the LDPE are gathered towards the central electrode within 100 seconds, as shown in Fig. 5e, f and Video S3 (ESI†). The maximum size of the LDPE powder sample is 80 mesh (about 120 μm), and the maximum diameter of single LDPE particle measured under an electron microscope agrees with this data, as shown in Fig. S20 (ESI†). However, based on the calculated velocity in Fig. S19d (ESI†), the LDPE particles would move rather slowly under the drive of only the DEP force. Considering the theoretical velocity and experimental results, the movement of LDPE particles towards central electrodes may be mainly driven by the EP force. For further confirmation of the driven force, a reverse high voltage is applied to the electrode by the reverse rotation of the SH-TENG, and the central electrode of the oil purification system is positively charged while the outer electrode is negatively charged. By stirring 100 mg of LDPE into transparent D-oil, a new cup of oil mixture is obtained. As shown in Fig. S21 (ESI†), after 100 s, most LDPE moved towards the wall of the beaker, which indicates that the EP force is the major driven force of the movement of LDPE particles. By measuring the light transmittance of the D-oil, we can estimate the residual situation of LDPE particles in the oil, as presented in Fig. S22 (ESI†). The transmittance of the pure oil is 100%, and the transmittance of the oil with 100 mg LDPE impurity particles is around 75%. After the purification treatment of the SH-TENG, the transmittance of the oil is increased to 99%, indicating that most of the particles suspended in the oil have been purified. In order to further estimate the purification rate, we take out 10 μL of the mixed oil and observe it under an electron microscope after purification. As shown in Fig. S23 (ESI†), only 1 particle remained in 10 μL oil, which means about 5000 particles (about 4.4 mg) remained after purification in 50 ml oil. Therefore, about 95.6 mg of LDPE particles were purified, and the purification rate reached 95.6%. Thus, both conductive particles and dielectric particles can be purified by the oil purification system driven by the SH-TENG with high efficiency. Meanwhile, the columnar electrode in the middle can be removed and be replaced. During the experiments, the columnar electrode is covered with a VHB tape and the particles are all attached on the tape. It is very easy to replace the dirty tape and to start the second purification for the residual particles. This is also the typical operation process of the commercial purification system. Considering other advantages of the SH-TENG system such as low cost, straightforward operation of

device and easy to achieve high voltage, this SH-TENG system is promising for various applications, such as recovery of heavy metals or very small particles in oil pollution treatment, as shown in Fig. 5g. Furthermore, the same high electrostatic field provided by the SH-TENG can also help to disperse the particles in oil. Hence, we developed a different method for oil agitation based on the SH-TENG. The oil agitation system consists of a bare copper needle and an aluminum round plate attached to the bottom of the cup (see Fig. S24a, ESI†). The needle is connected to accumulator A of the SH-TENG and the plate is linked to accumulator B. Under the drive of the SH-TENG, the umbrella-shaped electric field is generated, as described in Fig. S24b (ESI†). For demonstration, LDPE and D-oil are put into the cup, while the LDPE particles gradually rise up and finally mixed evenly in the oil within 10 seconds during the rotation of the SH-TENG (see Fig. S24c and Video S4, ESI†). These results indicate an optional method for mixing different materials in the chemical industry.

Application of SH-TENGs for dielectric elastomer actuators

Due to the effect of the Maxwell force, the dielectric elastomers show significant shape deformation under the applied high electric field and such deformation can be utilized to realize a DEA device, opening up various promising applications in artificial muscles and soft electronics.[60] The fabricated DEA device is shown in Fig. 6a, where the elastomer film is fixed on an acrylic frame (4 cm × 4 cm), and the circular electrodes (carbon grease) are applied on the top and bottom of the film. Each accumulator of the SH-TENG is connected to the corresponding circular electrodes, respectively, which establishes an integrated actuation system. The mechanical strain of the elastomer film is controlled by the rotation of the SH-TENG, as shown in the inset of Fig. 6a. The deformation strain, which is defined as the percentage of area change of DEA, gradually reaches its limit (about 56%) with the continuous rotation of the SH-TENG, and the actuated strain shows almost no relaxation due to the sustainable charge supply of the SH-TENG (see Fig. 6b, c and Video S5, ESI†). Then, the shrinkage of the DEA can be observed with the reverse rotation of the SH-TENG. Fig. S25a (ESI†) shows the dependence of actuated strain with different moving steps of the SH-TENG, where the rotation rate is about 10 rpm. The actuated strain of the DEA increases from 0% to 56% with the moving steps from 0 to 48 and the DEA is broken down with the moving steps of 60. Based on the results shown in Fig. 3c, we can approximately calculate the applied voltage on this DEA according to the rotation steps of the SH-TENG and the calculated results can be seen in Fig. S25b (ESI†). This actuated strain is much larger than that in the previous work with the common single-electrode TENG,[34] which confirms the superior driving capability of the SH-TENG. Various possible applications of this SH-TENG can be developed in the fields of smart actuators, micro robotics and so on.

Application of SH-TENGs for electrospinning

The high voltage used in the electrospinning process is a DC voltage ranging from several to tens of kilovolts. As a power
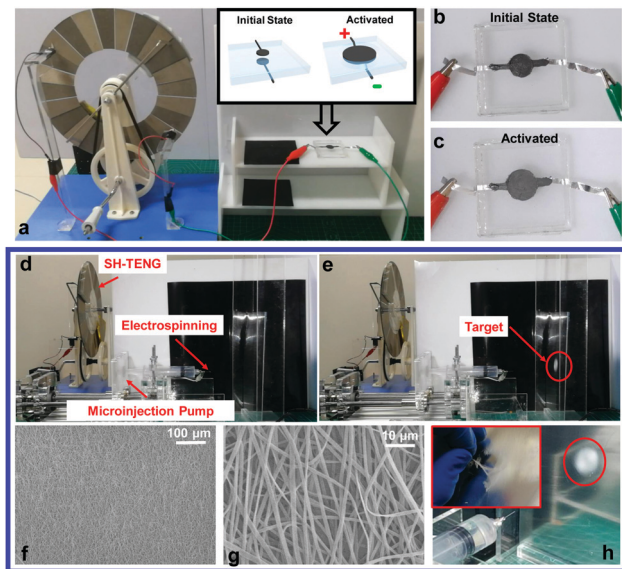
Fig. 6 Demonstration of the electrospinning system and elastomer driven by the SH-TENG. (a) Photograph of the elastomer driven by the SH-TENG, the inset demonstrates the deformation behavior caused by the SH-TENG. (b and c) Photograph of the elastomer at initial state and driven by the SH-TENG. (d and e) Photograph of the electrospinning system driven by the SH-TENG. After 30 s of manual operation of the SH-TENG (about 50 rpm), polymer nanofibers of PVA (target) are generated. (f and g) SEM image of the PVA nanofibers fabricated by the SH-TENG and the enlarged view (h) of fabricated PVA.

source with the unidirectional output characteristics and sustainable high voltage, the SH-TENG can be an ideal candidate to execute the electrospinning process directly without any external power source or multiplier circuits. This self-powered electrospinning system is composed of the SH-TENG, a syringe pump with PVA solution (9 wt%), and a simple spinneret. In this experiment, polyvinyl alcohol (PVA), a semi-crystalline and water-soluble polymer with good chemical and thermal stability, is chosen as the electrospinning solution.[61] Before the electrospinning process, the PVA solution is loaded in a syringe pump, accumulator A of the SH-TENG is connected to the needle tip, and accumulator B is connected to a piece of aluminum foil (to collect the electro-spun nanofibers). The detailed preparation of the electrospinning process is shown in the Experimental section. Fig. 6d and e are photographs before and after the operation of the SH-TENG. The electrospinning process of PVA is recorded using a normal digital camera (Video S6, ESI†). A consecutive Taylor cone is triggered by the system immediately with clockwise hand rotating of the SH-TENG, as shown in Fig. S26 (ESI†). The rotation speed of the SH-TENG is about 50 rpm and the generated voltage in the system should exceed at least 10 kV. Fig. 6f and g are the SEM images of the PVA nanofibers fabricated by operating the SH-TENG for 30 s, and Fig. 6h is the enlarged view of fabricated PVA nanofibers with a close-up of nanofibers in the inset. Based on the SEM observation, the nanofiber fabricated by the SH-TENG triggered the self-powered electrospinning system, which is comparable in quality to that fabricated by commercial electrospinning machines.[62] Previously, the multiplier rectifying

circuits are indispensable in the self-powered electrospinning system based on the TENG,[38] while our SH-TENG can directly drive the electrospinning system with a much lower rotation speed of the TENG. This experiment confirms the superior capability of this SH-TENG in comparison with previous strategy using multiplier circuits.

Conclusion

In summary, a SH-TENG based on a charge accumulation strategy to boost the output voltage was proposed, which can provide an unprecedented high-voltage output. Two charge accumulators with very small inherent capacitance were applied to establish very high electrostatic voltage and an array of transporting-electrodes on a rotating disk can help to transfer charges to accumulators, which can replenish the charge leakage from the accumulator. The combination of accumulators and transporting-electrodes can help to maintain ultrahigh voltage and a sustainable output voltage over 20 kV can be achieved, which allow this SH-TENG to continuously light up more than 8000 LEDs. The effects of the rotating speed and the central angle of electrodes on the performance of the SH-TENG are investigated, which shows the optimized performance can be realized with high speed (90 rpm) and a central angle of 1°. More importantly, the application of this SH-TENG can be extended to a new field of oil purification, owing to the sustainable high voltage. Combining with EP and DEP technology, a self-powered oil purify system is established, which can purify the suspended impurity particles of carbon and LDPE in 50 ml oil within 100 seconds, showing universal applicability for removing both conductive and dielectric particles. Similar effects can also be used for the oil agitation process to evenly mix the LDPE particles in the oil. This TENG-based oil purification system with a simple structure and zero power consumption offers a different approach for the oil recycling industry, which is consistent with the current theme of energy conservation and environmental protection. Moreover, two kinds of typical high-voltage devices, namely, the dielectric elastomer actuator (DEA) and electrospinning system, can be directly driven by this SH-TENG with a rather low rotation speed, which indicates a superior driving capability. By directly applying this SH-TENG to the DEA, a self-powered TENG-DEA system has been demonstrated to provide an expansion strain of 56%, showing great potential in the field of smart actuators or micro robotics. The self-powered electrospinning system driven by this SH-TENG also exhibits excellent performance in the manufacturing of PVA nanofibers, which is comparable with commercial electrospinning machines. The proposed SH-TENG as a stable ultrahigh-voltage source can also work for many other high-voltage applications such as electrostatic manipulation and air pollution treatment.

Experimental

The design of each part of SH-TENGs

The rotation disk consists of an acrylic plate with a diameter of 230 mm and a thickness of 3 mm. A center hole with a diameter

of 15 mm is designed on the disk. The two electrode arrays made of conductive cloth are attached on the disk. The outer radius of the single electrode is 113 mm, while the inner radius is 63 mm. The main part of the fan-shaped polarizer are two equal-sized dielectric films (Kapton and nylon). The outer radius of the dielectric film is 117 mm, and the inner radius is 51 mm. The transmission bridge consists of a copper ring with a cylindrical hole of 6 mm and two L-shaped copper bars with a length of 110 mm. The two copper bars are concentric, and they are symmetrically fixed on the outer side of the copper ring. The accumulator is a copper bar with a length of 20 mm and a diameter of 1.5 mm. The ends of the transmission bridge and accumulators all connect with flexible copper wires as mentioned above.

Fabrication of DEA

An acrylic elastomer (0.5 mm thick, VHB 4905, 3 M) was cut into 20×20 mm^2 sheets. The elastomer sheet was first stretched according to the pre-strain ratio ($\lambda = 2$, the ratio between the area of the elastomer film after (A') and before (A) stretching ($\lambda = A'/A$)), and then the film was fixed uniformly along a frame (40×40 mm^2). The circular areas at the center of the film were smeared with circular carbon grease (electrodes) on both the sides (electrode thickness: ≈ 80 μm). The electrodes were connected to the SH-TENG through a thin aluminum wire.

Preparation of the electrospinning process

The solution of the polymers used in the present work was a 9 wt% PVA. Then, the electrospinning solution was loaded in a 20 ml syringe with a 28-gauge needle tip, which was connected to accumulator A. With the injection rate of 0.15 ml h^{-1}, the solution was pumped out of the needle tip by a syringe pump. A piece of aluminum foil was connected to accumulator B to collect the PVA nanofiber, and the tip-to-collector distance was 10 cm.

Measurements

The electrical output performance was measured using an electrometer (Keithley 6514). The light transmittance of dimethyl silicone oil was measured using a spectrophotometer (Shimadzu UV 3600). The surface morphology of Kapton and nylon were inspected by scanning electron microscopy (Hitachi SU8020, Japan). The rotary process of disk was driven by a belt transmission mechanism, while the belt transmission mechanism was driven using a commercial stepper motor (51K120RGU-CF). We removed the handle from the large pulley of the belt transmission mechanism and connected the shaft of the motor with the shaft of the large pulley *via* coupling. The corresponding physical parameters of oil and particles are provided in Table S3 (ESI†).

Conflicts of interest

There are no conflicts to declare.

Acknowledgements

References

1 J. Chen, *et al.*, Micro-cable structured textile for simultaneously harvesting solar and mechanical energy, *Nat. Energy*, 2016, **1**, 16138.

2 R. Hinchet, *et al.*, Transcutaneous ultrasound energy harvesting using capacitive triboelectric technology, *Science*, 2019, **365**, 491–494.

3 J. W. Lee, *et al.*, Robust nanogenerators based on graft copolymers via control of dielectrics for remarkable output power enhancement, *Sci. Adv.*, 2017, **3**, e1602902.

4 W. Xu, *et al.*, A droplet-based electricity generator with high instantaneous power density, *Nature*, 2020, **578**, 392–396.

5 N. Zhang, *et al.*, Non-contact cylindrical rotating triboelectric nanogenerator for harvesting kinetic energy from hydraulics, *Nano Res.*, 2020, DOI: 10.1007/s12274-020-2654-7.

6 F. Wen, *et al.*, Battery-free short-range self-powered wireless sensor network (SS-WSN) using TENG based direct sensory transmission (TDST) mechanism, *Nano Energy*, 2019, **67**, 104266.

7 H. Guo, *et al.*, A highly sensitive, self-powered triboelectric auditory sensor for social robotics and hearing aids, *Sci. Robot.*, 2018, **3**, eaat2516.

8 J. Wang, *et al.*, Self-powered electrowetting optical switch driven by a triboelectric nanogenerator for wireless sensing, *Nano Energy*, 2019, **66**, 104140.

9 Y. Tang, *et al.*, Triboelectric Touch-Free Screen Sensor for Noncontact Gesture Recognizing, *Adv. Funct. Mater.*, 2020, **30**, 1907893.

10 J. Chen, *et al.*, Actuation and sensor integrated self-powered cantilever system based on TENG technology, *Nano Energy*, 2019, **64**, 103920.

11 Y. Lee, *et al.*, Transparent and attachable ionic communicators based on self-cleanable triboelectric nanogenerators, *Nat. Commun.*, 2018, **9**, 1804.

12 B. Zhang, *et al.*, Breath-based human–machine interaction system using triboelectric nanogenerator, *Nano Energy*, 2019, **64**, 103953.

13 S. S. Kwak, *et al.*, Butylated melamine formaldehyde as a durable and highly positive friction layer for stable, high output triboelectric nanogenerators, *Energy Environ. Sci.*, 2019, **12**, 3156–3163.

14 K. Parida, *et al.*, Extremely stretchable and self-healing conductor based on thermoplastic elastomer for all-three-dimensional printed triboelectric nanogenerator, *Nat. Commun.*, 2019, **10**, 2158.

15 J. Shao, *et al.*, Quantifying the power output and structural figure-of-merits of triboelectric nanogenerators in a charging system starting from the Maxwell's displacement current, *Nano Energy*, 2019, **59**, 380–389.

16 H. R. Lee, *et al.*, Stretchable Ionics–a promising candidate for upcoming wearable devices, *Adv. Mater.*, 2018, **30**, 1704403.

17 Y. Mao, *et al.*, A paper triboelectric nanogenerator for self-powered electronic systems, *Nanoscale*, 2017, **9**, 14499–14505.

18 Z. L. Wang, On Maxwell's displacement current for energy and sensors: the origin of nanogenerators, *Mater. Today*, 2017, **20**, 74–82.

19 J. Nie, *et al.*, Power generation from the interaction of a liquid droplet and a liquid membrane, *Nat. Commun.*, 2019, **10**, 1–10.

20 X. Chen, *et al.*, Transparent and stretchable bimodal triboelectric nanogenerators with hierarchical micro-nanostructures for mechanical and water energy harvesting, *Nano Energy*, 2019, **64**, 103904.

21 Y. Liu, *et al.*, Thin, Skin-Integrated, Stretchable Triboelectric Nanogenerators for Tactile Sensing, *Adv. Electron. Mater.*, 2019, **6**, 1901174.

22 G. Liu, *et al.*, Wireless electric energy transmission through various isolated solid media based on triboelectric nanogenerator, *Adv. Energy Mater.*, 2018, **8**, 1703086.

23 M. Wang, *et al.*, Air-Flow-Driven Triboelectric Nanogenerators for Self-Powered Real-Time Respiratory Monitoring, *ACS Nano*, 2018, **12**, 6156–6162.

24 S. Li, *et al.*, Manipulating the triboelectric surface charge density of polymers by low-energy helium ion irradiation/implantation, *Energy Environ. Sci.*, 2020, **13**, 896–907.

25 J. W. Lee, *et al.*, High-Output Triboelectric Nanogenerator Based on Dual Inductive and Resonance Effects-Controlled Highly Transparent Polyimide for Self-Powered Sensor Network Systems, *Adv. Energy Mater.*, 2019, **9**, 1901987.

26 H.-J. Yoon, *et al.*, 3D-printed biomimetic-villus structure with maximized surface area for triboelectric nanogenerator and dust filter, *Nano Energy*, 2019, **63**, 103857.

27 X. Chen, *et al.*, Hybrid generator based on freestanding magnet as all-direction in-plane energy harvester and vibration sensor, *Nano Energy*, 2018, **49**, 51–58.

28 L. Zheng, *et al.*, Self-Powered Electrostatic Actuation Systems for Manipulating the Movement of both Microfluid and Solid Objects by Using Triboelectric Nanogenerator, *Adv. Funct. Mater.*, 2017, **27**, 1606408.

29 J. Nie, *et al.*, Electrically responsive materials and devices directly driven by the high voltage of triboelectric nanogenerators, *Adv. Funct. Mater.*, 2018, **29**, 1806351.

30 J. Nie, *et al.*, Self-powered microfluidic transport system based on triboelectric nanogenerator and electrowetting technique, *ACS Nano*, 2018, **12**, 1491–1499.

31 L. Xu, *et al.*, Ultrahigh charge density realized by charge pumping at ambient conditions for triboelectric nanogenerators, *Nano Energy*, 2018, **49**, 625–633.

32 W. Ding, *et al.*, TriboPump: A Low-Cost, Hand-Powered Water Disinfection System, *Adv. Energy Mater.*, 2019, **9**, 1901320.

33 S. Wang, *et al.*, Freestanding Triboelectric-Layer-Based Nanogenerators for Harvesting Energy from a Moving Object or Human Motion in Contact and Non-contact Modes, *Adv. Mater.*, 2014, **26**, 2818–2824.

34 X. Chen, *et al.*, Stimulating Acrylic Elastomers by a Triboelectric Nanogenerator – Toward Self-Powered Electronic Skin and Artificial Muscle, *Adv. Funct. Mater.*, 2016, **26**, 4906–4913.

35 W. Liu, *et al.*, Integrated charge excitation triboelectric nanogenerator, *Nat. Commun.*, 2019, **10**, 1–9.

36 W. Liu, *et al.*, Switched-capacitor-convertors based on fractal design for output power management of triboelectric nanogenerator, *Nat. Commun.*, 2020, **11**, 1–10.

37 L. Xu, *et al.*, Giant Voltage Enhancement via Triboelectric Charge Supplement Channel for Self-Powered Electroadhesion, *ACS Nano*, 2018, **12**, 10262–10271.

38 C. Li, *et al.*, Self-Powered Electrospinning System Driven by a Triboelectric Nanogenerator, *ACS Nano*, 2017, **11**, 10439–10445.

39 H. Huo, *et al.*, Triboelectric nanogenerators for electro-assisted cell printing, *Nano Energy*, 2020, **67**, 104150.

40 G. Zhu, *et al.*, Radial-arrayed rotary electrification for high performance triboelectric generator, *Nat. Commun.*, 2014, **5**, 3426.

41 C. Wu, *et al.*, Triboelectric Nanogenerator: A Foundation of the Energy for the New Era, *Adv. Energy Mater.*, 2019, **9**, 1802906.

42 X. Chen, *et al.*, Self-powered modulation of elastomeric optical grating by using triboelectric nanogenerator, *Nano Energy*, 2017, **38**, 91–100.

43 X. Wang, *et al.*, A flexible triboelectric-piezoelectric hybrid nanogenerator based on P (VDF-TrFE) nanofibers and PDMS/MWCNT for wearable devices, *Sci. Rep.*, 2016, **6**, 36409.

44 X. Chen, *et al.*, Self-Powered Trace Memorization by Conjunction of Contact-Electrification and Ferroelectricity, *Adv. Funct. Mater.*, 2015, **25**, 739–747.

45 G. Q. Gu, *et al.*, Triboelectric nanogenerator enhanced nanofiber air filters for efficient particulate matter removal, *ACS Nano*, 2017, **11**, 6211–6217.

46 Y. Zi, *et al.*, Field Emission of electrons powered by a triboelectric nanogenerator, *Adv. Funct. Mater.*, 2018, **28**, 1800610.

47 A. Li, *et al.*, Triboelectric nanogenerators for sensitive nanocoulomb molecular mass spectrometry, *Nat. Nanotechnol.*, 2017, **12**, 481.

48 D. A. Bikos, *et al.*, Band-collision gel electrophoresis, *Nat. Commun.*, 2019, **10**, 3631.

49 A. M. Brooks, *et al.*, Shape-directed rotation of homogeneous micromotors via catalytic self-electrophoresis, *Nat. Commun.*, 2019, **10**, 495.

50 H. A. Pohl, *et al.*, Dielectrophoretic force, *J. Theor. Biol.*, 1972, **37**, 1–13.

51 S.-H. Cha, *et al.*, Fabrication of nanoribbons by dielectrophoresis assisted cold welding of gold nanoparticles on mica substrate, *Sci. Rep.*, 2019, **9**, 3629.

52 Q. Wang, *et al.*, Microfluidic dielectrophoresis illuminates the relationship between microbial cell envelope polarizability and electrochemical activity, *Sci. Adv.*, 2019, **5**, eaat5664.

53 H. Zou, *et al.*, Quantifying the triboelectric series, *Nat. Commun.*, 2019, **10**, 1427.

54 C. Chiang Foo, *et al.*, Model of dissipative dielectric elastomers, *J. Appl. Phys.*, 2012, **111**, 034102.

55 T. I. Lee, *et al.*, High-Power Density Piezoelectric Energy Harvesting Using Radially Strained Ultrathin Trigonal Tellurium Nanowire Assembly, *Adv. Mater.*, 2013, **25**, 2920–2925.

56 C. Zhang, *et al.*, Theoretical Comparison, Equivalent Transformation, and Conjunction Operations of Electromagnetic Induction Generator and Triboelectric Nanogenerator for Harvesting Mechanical Energy, *Adv. Mater.*, 2014, **26**, 3580–3591.

57 X. Wang, *et al.*, Triboelectric Nanogenerator Based on Fully Enclosed Rolling Spherical Structure for Harvesting Low-Frequency Water Wave Energy, *Adv. Energy Mater.*, 2015, **5**, 1501467.

58 H. A. Pohl, Some Effects Of Nonuniform Fields On Dielectrics, *J. Appl. Phys.*, 1958, **29**, 1182–1188.

59 H. A. Pohl, *et al.*, Continuous Separations Of Suspensions By Nonuniform Electric Fields In Liquid Dielectrics, *J. Electrochem. Soc.*, 1960, **107**, 390–396.

60 X. Chen, *et al.*, Tunable Optical Modulator by Coupling a Triboelectric Nanogenerator and a Dielectric Elastomer, *Adv. Funct. Mater.*, 2017, **27**, 1603788.

61 C. Shao, *et al.*, Fiber mats of poly (vinyl alcohol)/silica composite via electrospinning, *Mater. Lett.*, 2003, **57**, 1579–1584.

62 A. Koski, *et al.*, Effect of molecular weight on fibrous PVA produced by electrospinning, *Mater. Lett.*, 2004, **58**, 493–497.